Effect of caudal fin flexibility on the propulsive efficiency of a fish-like swimmer

2014 Bioinspir. Biomim. 9 046001

(http://iopscience.iop.org/1748-3190/9/4/046001)

IOP Publishing Bioinspiration & Biomimetics
Bioinspir. Biomim. 9 (2014) 046001 (12pp) doi:10.1088/1748-3182/9/4/046001

Effect of caudal fin flexibility on the propulsive efficiency of a fish-like swimmer

M Bergmann[1,2], A Iollo[1,2] and R Mittal[3]

[1] Inria, F-33400 Talence, France
[2] University of Bordeaux, IMB, UMR 5251, F-33400 Talence, France
[3] Department of Mechanical Engineering, Johns Hopkins University, Baltimore, MD 21218, USA

E-mail: michel.bergmann@inria.fr

Received 3 June 2014, revised 16 July 2014
Accepted for publication 1 August 2014
Published 25 September 2014

Abstract

A computational model is used to examine the effect of caudal fin flexibility on the propulsive efficiency of a self-propelled swimmer. The computational model couples a penalization method based Navier–Stokes solver with a simple model of flow induced deformation and self-propelled motion at an intermediate Reynolds number of about 1000. The results indicate that a significant increase in efficiency is possible by careful choice of caudal fin rigidity. The flow-physics underlying this observation is explained through the use of a simple hydrodynamic force model and guidelines for bioinspired designs of flexible fin propulsors are proposed.

Keywords: propulsive efficiency, fish-like swimming, computational model

(Some figures may appear in colour only in the online journal)

1. Introduction

Investigation of swimming hydrodynamics can on the one hand provide insights into biological evolution and physiology, and on the other, lead to new bioinspired designs of underwater vehicles. Quantitative evaluation of the mechanical and fluid dynamical characteristics of swimming in experiments is challenging (Triantafyllou *et al* 2000, Wen and Lauder 2013). In particular, precise control of the kinematics and dynamics of the experimental model is difficult; harder still is the accurate measurement of forces and power of a freely swimming model. In this regard, computational modeling and simulation is well suited for such investigation. However, three-dimensional numerical simulation of swimming modes have only become viable in the last decade (Mittal *et al* 2008, Shirgaonkar *et al* 2009, Curet *et al* 2010, Hieber and Koumoutsakos 2008, Gazzola *et al* 2011) due to the significant complexity and computational expense involved in such simulations.

The bending of biological propulsive structures is well known (McCutchen 1970). Here, we thus use numerical simulation to study this specific aspect of fish-like swimming: the influence of caudal fin flexibility on the swimming performance of the so called 'carangiform' mode of swimming (Sfatiotakis *et al* 1999). A number of past numerical (Dong *et al* 2010, Ramamurti *et al* 2002) and experimental (Lauder *et al* 2006, Esposito *et al* 2011) studies have examined the effect of pectoral fin deformation on labriform propulsion. However, there have been few examinations that have quantified the degree of flexibility with increase in efficiency (Bose 1995, Prempraneerach *et al* 2003, Vermeiden *et al* 2012, Katz and Weihs 1978, Heathcote *et al* 2008). Esposito *et al* (2011) found that there exist optimal fin flexural rigidity for maximizing thrust at fixed point, i.e., for a flapping fin that is not displacing. Thiria and Godoy-Diana (2010) have also shown that flexible wings can lead to substantial reduction in the consumed power and to an increment of the propulsive force, also for a fixed point. Marais *et al* (2012) observed a thrust enhancement by a factor three for a fixed flexible pitching foil compared to the rigid case. Vanella *et al* (2009) have used a simple two-link model to investigate the potential benefits of flexibility and highlighted the importance of considering nonlinear resonances for enhancing aerodynamic performance.

Recent literature, see for example (Spagnolie *et al* 2010, Masoud and Alexeev 2010), suggests that resonance play an essential role in determining optimal propulsion efficiency. Experimental and numerical evidence presented in these papers support the conclusion that optimal flapping performance is obtained for foil flexibility maximizing tip

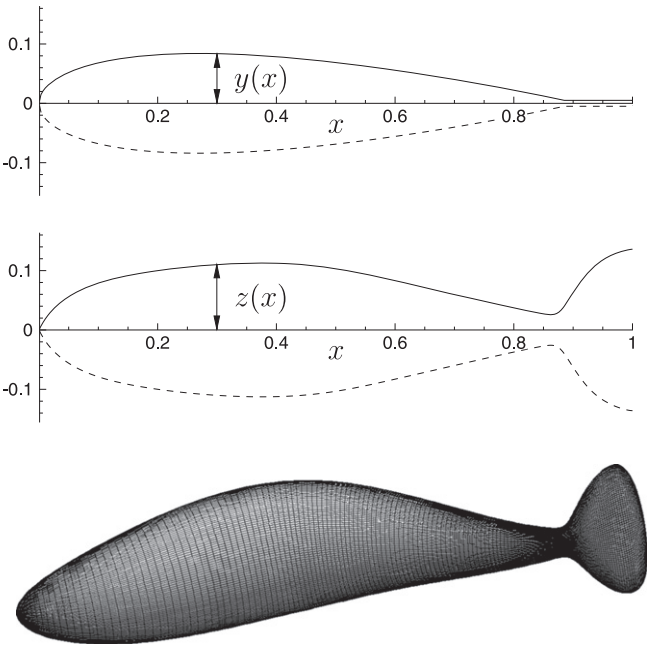

Figure 1. Representation of the elliptical axes $y(x)$ and $z(x)$ defining the fish shape.

deformation for given forcing. Hence, resonance determines optimal lift and efficiency characteristics for given flapping kinematics. On the other hand, Ramananarivo *et al* (2011) experimentally show that aerodynamic flow optimization may prevail on resonance considerations in selecting optimal wing shape and hence optimal flexibility. Also Liu *et al* (2013) investigated power efficiency modification for flapping wing energy devices. They found that the flexible structure of a wing is beneficial to enhance power efficiency of tidal energy harvesting devices. Finally, Young *et al* (2009) have examined the influence of insect wing deformation on the flight efficiency thanks to both numerical and experimental studies, highlighting the role of curvature on efficiency.

Similar studies have not been undertaken for caudal-fin propulsion of a self-propelled swimmer. The vast majority of fishes and marine mammals (especially those that can swim fast) employ their caudal fin for propulsion and it is therefore expected that an analysis of this propulsion mode will yield useful insights for the design of bioinspired swimming vehicles. It is well known that flow patterns over the body as well as in the wake significantly influence swimming performance (Fish and Lauder 2006, Zhu *et al* 2002). These patterns are in turn influenced by the geometry of the body as well as its kinematics. A number of past studies have examined these effects of body geometry as well as prescribed body and/or fin kinematics (Mittal *et al* 2008, Borazjani and Sotiropoulos 2008, Shirgaonkar *et al* 2009, Curet *et al* 2010, Hieber and Koumoutsakos 2008, Borazjani and Sotiropoulos 2009, Gazzola *et al* 2011). In the current study we focus on the efficiency improvement in a self-propelled 'fish' obtained by a simple and local modification of the flexural rigidity of the caudal fin. We evaluate the swimming efficiency by employing a non-dimensional index that takes into account the total mechanical power acting on the fluid, the modeled fish velocity and the force exerted in the direction of locomotion (von Loebbecke *et al* 2009, Borazjani and Sotiropoulos 2008). We concentrate on locomotion at low Reynolds numbers so that all the relevant scales of the flow are well resolved in these three-dimensional simulations.

2. Numerical modeling

The modeling of the flow past a deformable body and the numerical method employed (§2.1) are basically the same as those described in Mittal *et al* (2008) and Bergmann and Iollo (2011) and we only provide a brief description of the salient features.

2.1. Flow around deformable bodies

The flow is modeled by the incompressible Navier–Stokes equations. The kinematics of the deforming body are prescribed. The kinematics of the caudal fin can either be prescribed or computed from a unidirectional flow-induced deformation model. The trajectory of the modeled fish is computed from the integral force and torque exerted on the swimmer surface. The displacement of the swimmer across the domain is implemented via Lagrangian markers that are attached to the swimmer surface. The domain under consideration is a three-dimensional box $\Omega = \Omega_f \cup \Omega_s$ (the 'aquarium'), where Ω_f is the domain filled by fluid, and Ω_s is the domain defined by the swimmer. The outer boundary and the swimmer surface are denoted by $\partial\Omega_f$ and $\partial\Omega_s$ respectively. Given this, the governing incompressible Navier–Stokes equations are given by

$$\rho\left(\frac{\partial \boldsymbol{u}}{\partial t} + (\boldsymbol{u}\cdot\nabla)\boldsymbol{u}\right) = -\nabla p + \mu\Delta\boldsymbol{u} \text{ in } \Omega_f, \quad (1)$$

$$\nabla\cdot\boldsymbol{u} = 0 \text{ in } \Omega_f, \quad (2)$$

with initial conditions $\boldsymbol{u}(\boldsymbol{x},\ 0) = \boldsymbol{u}_0(\boldsymbol{x})$ in Ω_f, boundary conditions $\boldsymbol{u}(\boldsymbol{x},\ t) = \boldsymbol{0}$ on $\partial\Omega_f$ and $\boldsymbol{u}(\boldsymbol{x},\ t) = \boldsymbol{u}_s(\boldsymbol{x},\ t)$ on $\partial\Omega_s$. Equations (1) and (2) are discretized in time with a second-order projection scheme (Chorin 1968) and spatially discretized on a fixed Cartesian mesh with grid spacing of $\Delta x = \Delta y = \Delta z = h$. Since the swimmer boundary $\partial\Omega_s$ is curvilinear the Cartesian mesh does not conform to this boundary; the boundary conditions $\boldsymbol{u}(\boldsymbol{x},\ t) = \boldsymbol{u}_s(\boldsymbol{x},\ t)$ on $\partial\Omega_s$ are therefore imposed using a discrete forcing immersed boundary method and penalization (Mittal and Iaccarino 2005, Mittal *et al* 2008, Bergmann and Iollo 2011).

2.2. Modeled fish geometry and deformation

We consider a prototype swimmer of unit length, $\ell = 1$ m. At rest, the midline (backbone) of the fish-like geometry coincides with $0 \leqslant x \leqslant 1$, $y = z = 0$. This backbone is then discretized by 'vertebra' located at x_i for $i = 1,..,N$. The three-dimensional fish-like shape is reconstructed using N ellipses with minor-axes $y(x_i)$ and $z(x_i)$. These axes lengths are found

using B-splines (see figure 1). The maximum transverse dimensions are $2\,y = 0.17$ and $2\,z = 0.24$ and the caudal fin has a maximal vertical span $2\,z = 0.25$. These values are chosen to approximately mimic the MIT robot bluefin tuna (Barrett *et al* 1999). The final swimmer geometry is presented in figure 1.

The shape of the swimming body is obtained by deforming the body midline in the plane $z = 0$ as a function of time while keeping each elliptic cross section to be orthogonal to the midline during deformation. The body surface is discretized as $\partial\Omega_s = \cup_{i=1}^{N_s} \partial\Omega_s^i$, where N_s denotes the number of surface sections and $\partial\Omega_s^i$ defines a covering space of the surface. The velocity of each surface element, noted $\boldsymbol{u}_s(\boldsymbol{x}_i,\ t)$, is then computed by tracking the Lagrangian markers corresponding to each surface element for $i = 1\,,..N_s$.

Based on previous work, the deformation of the midline is based on a traveling wave with a space-dependent amplitude (Barrett *et al* 1999, Bergmann and Iollo 2011) as

$$y_{\text{mid}}(x) = a(x)\sin(kx - \omega t), \tag{3}$$

where $k = 2\pi/\lambda$ denotes the wave number associated with a wavelength λ and $\omega = 2\pi f$ denotes the pulsation of the oscillations associated with frequency f. The amplitude envelope $a(x) = c_0 + c_1 x + c_2 x^2$ is usually defined by three parameters c_0, c_1 and c_2 that can be adjusted. There is one constraint (the back bone length) and four independent parameters: c_0, c_1, c_2 and the abscissa of the tail extremity. Therefore we have the possibility of choosing three of these parameters and to determine the last thanks to the constraint. We reach a desired maximal tail excursion denoted by A, while the backbone length remains $\ell = 1$ m. In what follows we will take $c_0 = c_2 = 0$ and $c_1 = 0.1$. These values correspond to a linear growth of the backward traveling wave and result in a swimming law that qualitatively agrees with those

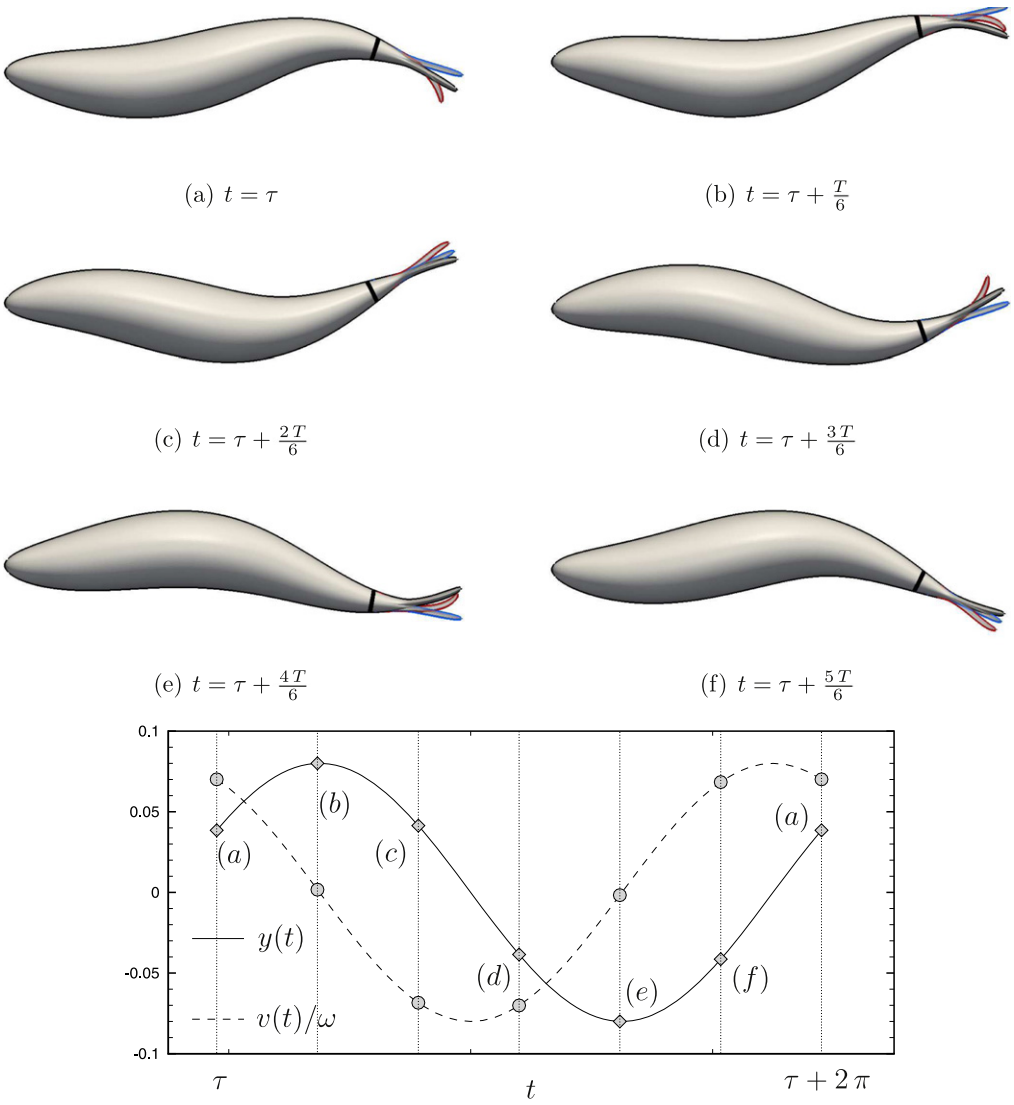

Figure 2. Deformation of the swimmer over one swimming stroke T (corresponding to a frequency $f = 2.0$ Hz). The same sinusoidal swimming law is applied on the whole shape except between the black section and the tail extremity where an elastic model is applied in the blue and red case. The black shape corresponds to an imposed tail deformation, the blue shape corresponds to a rigid tail and the red shape corresponds to a flexible tail. The bottom figure represents position and vertical velocity of the section marked in black.

observed in Trachurus. However, these are not the values necessarily observed in a specific actual fish swimming.

Without action of external forces the center-of-mass of the swimmer should not move. To respect this constraint, after deforming the swimmer as explained above, we subtract the motion of the center-of-mass from the displacement of each Lagrangian marker on the fish surface.

2.3. Caudal fin modeling

The primary objective here is to assess the effect of caudal fin flexibility on swimming performance. To this end, the deformation can be either imposed on the whole midline length including the caudal fin (black shape shown in figure 2), or only on the portion excluding the caudal fin (which extends over the last 20% of the midline, see red or blue shapes in figure 2). For these latter cases, we model the fin by a lumped parameter elastic medium, similarly to what is done in (Wiens and Nahon 2012) for snake-like swimmers. The elastic caudal tail is composed by rigid struts joined by elastic links. Each link is subject to a couple C_i that is proportional to the square of the local tangential speed V_{i+1} of the next junction. This couple is a crude approximation of the hydrodynamic local force exerted by the fluid on the structure. In section 4 we will show that this hypothesis is approximatively verified in our simulations.

To further simplify the model, we assume that the angles are small and the inertia and hydrodynamic forces balance for the struts following the one considered. Then, we have

$$\ddot{\theta}_i + \beta\dot{\theta}_i + k\theta_i = C_i, \quad i = 1\,,..N_L - 1,$$

where θ_i is the rotation angle with respect to the previous strut, $C_i = -\alpha|V_{i+1}|V_{i+1}$, N_L is the number of links, $V_i = V_0 + i\,l\,(\dot{\theta}_0 + \sum_{k=1}^{i}\dot{\theta}_k)$, l is the length of the struts. The point $i = 0$ corresponds to 0.8 of the midline and is the last point where the deformation is explicitly imposed by (3), so that V_0 and $\dot{\theta}_0$ are given functions of time. This equation corresponds to a classical spring-damper system with a forcing term that couples the system. The angular acceleration of a strut with respect to the previous is proportional to the sum of the couple exerted on the strut, the elastic force and the damping force. The initial condition is $\theta_i = 0$, $\forall i$. In the following examples we let $\beta = 1$, $10^3 \leqslant k \leqslant 10^4$, $0 \leqslant \alpha \leqslant 16 \times 10^{-2}$ and $N_L = 60$. These parameters were selected to obtain a realistic deformation of the tail, as in figure 2. The effect of elastic recoil and energy storage in the tail trajectory can be observed: the elastic tail is always lagging behind the rigid tail as expected, whereas it can either overcome or lag behind the imposed motion tail.

In the following we will study the effect of the model parameters k and α on swimming efficiency. By varying k we modify the rigidity of the springs and hence the characteristic frequencies of the whole structure. When α is modified, we increase or decrease the intensity of the source term so that the structure deformations are increased or decreased by keeping the same characteristic frequencies of the structure. This will allow us to select an optimal k corresponding to maximum tail amplitudes for given forcing. For fixed k a similar effect on flexibility is obtained by varying α, keeping the ratio of inertia to rigidity (and hence the structure characteristic frequencies) constant.

In summary, this crude model keeps the essential features of a viscoelastic structure, such as elastic recoil and velocity damping, mimicking the feed-back effects of actual fluid forces via the terms C_i.

2.4. Force, torque and power

Let the dimensionless stress tensor $\mathbb{T}(\boldsymbol{u},\ p) = -p\boldsymbol{I} + \frac{1}{\mathrm{Re}}(\nabla\boldsymbol{u} + \nabla\boldsymbol{u}^T) = -p\boldsymbol{I} + \boldsymbol{\tau}$ and $\boldsymbol{n}$ the unit outward vector to $\partial\Omega_s$, then the forces and the torques exerted by the fluid onto the bodies are

$$\begin{aligned}\boldsymbol{F}_s &= -\int_{\partial\Omega_s}\mathbb{T}(\boldsymbol{u},\ p)\boldsymbol{n}\,\mathrm{d}\boldsymbol{x},\\ \boldsymbol{M}_s &= -\int_{\partial\Omega_s}\boldsymbol{r}_G\wedge(\mathbb{T}(\boldsymbol{u},\ p)\boldsymbol{n})\mathrm{d}\boldsymbol{x},\end{aligned} \tag{4}$$

with $\boldsymbol{r}_G = \boldsymbol{x} - \boldsymbol{x}_G$ ($\boldsymbol{x}_G$ center of mass). Since the boundary $\partial\Omega_s$ does not fit the computational mesh that will be employed, $\boldsymbol{u}$ and p are obtained using Lagrange interpolation. These forces and torques are used to compute the swimmer displacement. The velocity at the swimmer surface is

$$\boldsymbol{u}_s = \bar{\boldsymbol{u}} + \boldsymbol{u}^\theta + \tilde{\boldsymbol{u}}, \tag{5}$$

where $\tilde{\boldsymbol{u}}$ is the imposed deformation velocity, $\bar{\boldsymbol{u}}$ is the translation velocity and $\boldsymbol{u}^\theta$ is the rigid rotation velocity. The translation velocity can be computed from the forces $\boldsymbol{F}_s$ by $m\frac{\mathrm{d}\bar{\boldsymbol{u}}_s}{\mathrm{d}t} = \boldsymbol{F}_s$, m being the body mass. The rotation velocity is given by $\boldsymbol{u}_s^\theta = \boldsymbol{\Theta}_s \times \boldsymbol{r}_G$. The angular velocity $\boldsymbol{\Theta}_s$ is obtained from the torques $\boldsymbol{M}_s$ by solving $\frac{\mathrm{d}J\boldsymbol{\Theta}_s}{\mathrm{d}t} = \boldsymbol{M}_s$, where J denoted the body inertia matrix.

The force exerted by the fluid on the body surface segment $\partial\Omega_s^i$ is

$$\boldsymbol{F}^i = \left(F_x^i,\ F_y^i,\ F_z^i\right)^T = -\int_{\partial\Omega_s^i}\mathbb{T}(\boldsymbol{u},\ p)\cdot\boldsymbol{n}\,\mathrm{d}\boldsymbol{x},$$

where $\boldsymbol{n}$ the unit outward vector to $\partial\Omega_s^i$. The total work done over one stroke T is then

$$W_{\mathrm{total}} = \int_T\sum_{i=1}^{N_s}\boldsymbol{F}^i\cdot\boldsymbol{u}^i\,\mathrm{d}t, \tag{6}$$

where $\boldsymbol{u}^i$ is the average velocity on the surface $\partial\Omega_s^i$. The useful work is defined as the part of the total work that is done by the hydrodynamic force exerted in the direction of swimming (von Loebbecke *et al* 2009). For instance, if the swimmer velocity is positive in the x-direction, $U_x > 0$, then the useful work is given by

$$W_{\mathrm{useful}} = \int_T\sum_{i=1}^{N_s}\frac{\left(F_x^i - p_0\,n_x\right) + \left|F_x^i - p_0\,n_x\right|}{2}\,U_x^i\,\mathrm{d}t. \tag{7}$$

where p_0 is the reference static pressure used to compute $\mathbb{T}$ and hence $\boldsymbol{F}^i$. The propulsive efficiency can then be defined

as

$$\eta = \frac{W_{\text{useful}}}{W_{\text{total}}}. \tag{8}$$

The definition of efficiency is not unique, according to possibly different specific propulsion objectives. A definition that is closer to classic Froude propulsive efficiency is proposed for example in Borazjani and Sotiropoulos (2008)

$$\eta_f = \frac{T_x U_x}{T_x U_x + P_l}, \tag{9}$$

where

$$T_x = -\int_T \sum_{i=1}^{N_s} \frac{-p\, n_x + |p\, n_x|}{2}\, \mathrm{d}t - \int_T \sum_{i=1}^{N_s} \frac{(\boldsymbol{\tau}\, n)_x + |(\boldsymbol{\tau}\, n)_x|}{2}\, \mathrm{d}t; \tag{10}$$

and P_l is the power of the forces in the lateral direction. We will see that in this context the results provided by these two definitions are similar in terms of optimality of caudal fin flexibility.

3. Numerical validations

The numerical method employed has been extensively validated for several 2D test cases in Bergmann and Iollo (2011). In what follows, 3D validations are presented. We first study the terminal velocity of a sphere falling under gravity. Then we perform a convergence study of the terminal velocity of a swimming fish with respect to spatial discretization. Finally, we show that the assumption $C_i = -\alpha |V_{i+1}| V_{i+1}$ is reasonably verified for swimming laws similar to those investigated later in this paper.

3.1. Sedimentation of a sphere

Both experimental (Clift *et al* 1978) and numerical (Glowinski *et al* 2001, Coquerelle and Cottet 2008) results are found in the literature for the sedimentation of a sphere under the gravity. The sketch of the configuration is given in figure 3. We chose the same non-dimensional parameters as Coquerelle and Cottet (2008), the sphere (diameter D) falls under gravity in an vertical cylinder (diameter $L = 1$) filled with a fluid of viscosity ν under the gravity $g = -980$. We model an infinite cylinder and impose homogeneous Neumann boundary conditions ($\frac{\partial \boldsymbol{u}}{\partial \boldsymbol{n}} = \boldsymbol{0}$, where $\boldsymbol{n}$ is the outward normal unit vector) at the top and bottom boundaries, respectively Γ_T and Γ_B. No slip boundary conditions, $\boldsymbol{u} = \boldsymbol{0}$, are imposed on the cylinder lateral boundary, Γ_L, using penalization (Angot *et al* 1999). Table 1 presents a comparison between terminal velocities for various diameters and viscosities. The terminal velocity, U, computed in this study is compared with experimental results U_E obtained by Clift *et al* (1978) and numerical results U_G and U_C obtained by Glowinski *et al* (2001) and Coquerelle and Cottet (2008) respectively. The results reported in table 1 are computed with a spatial discretization $h = 1/100$. Our results are comparable to those in the literature. These are typical results for several computational set up parameters.

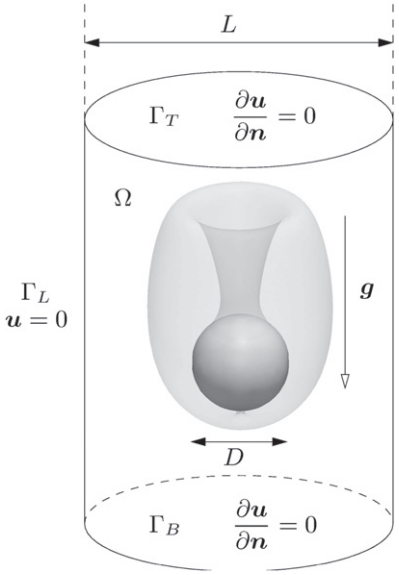

Figure 3. Sketch of a sphere sedimentation, with an example of isovorticity representation.

Table 1. Comparison between terminal velocities for spheres falling in a fluid for various diameters and viscosities.

D	ν	U_E	U_G	U_C	U
0.2	0.10	0.2571	0.2567	0.256	0.266
0.2	0.05	0.4603	0.4844	0.475	0.497
0.2	0.02	0.9129	0.9480	0.937	0.953
0.3	0.10	0.4047	0.4072	0.401	0.420
0.3	0.05	0.7493	0.7599	0.748	0.764
0.3	0.02	1.4359	1.3920	1.390	1.472

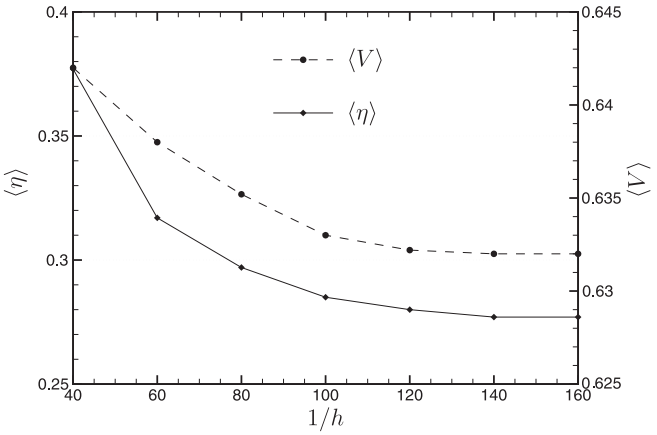

Figure 4. Convergence study of the swimmer velocity $\langle V \rangle$ the efficiency $\langle \eta \rangle$ versus the grid size $(1/h)$. The brackets denote an averaging operator.

3.2. Swimming velocity convergence

We perform a convergence study for a unitary length swimmer with respect to the grid size. The kinematic viscosity is set to 10^{-3} m^2 s^{-1}. The two quantities under consideration are the forward velocity $\langle V \rangle$ and the efficiency $\langle \eta \rangle$ ($\langle\langle \cdot \rangle\rangle$ denotes an averaging operator acting on a given number of periods when asymptotic velocity is reached). Figure 4 shows the evolutions of the swimmer velocity norm and efficiency (averaging on the last stroke period) versus the grid size $1/h$ (here, we have $h = \Delta x = \Delta y = \Delta z$). The swimming law (3) is imposed on the whole body with $c_1 = 0.1$, $c_0 = c_2 = 0$, $\lambda = 1$ m and $f = 2$ Hz. Both velocity and efficiency tend to converge toward limit values for fine meshes. Obviously, accuracy is improved with mesh size. However, the case $h = 1/120$ is a good compromise between accuracy and computation costs. Indeed, the errors between $h = 1/120$ and $h = 1/160$ are about 2% and $h = 1/120$ requires half CPU time than $h = 1/160$. We then set our spatial resolution to $h = 1/120$ for the following simulations. The domain under consideration is $x \in [-2, 6]$, $y \in [-2, 2]$ and $z \in [-2, 2]$. The finest mesh is then composed by $8 \times 4 \times 4 \times 160^3 \approx 5 \times 10^8$ mesh nodes. We considered the physical domain as an aquarium and imposed thus

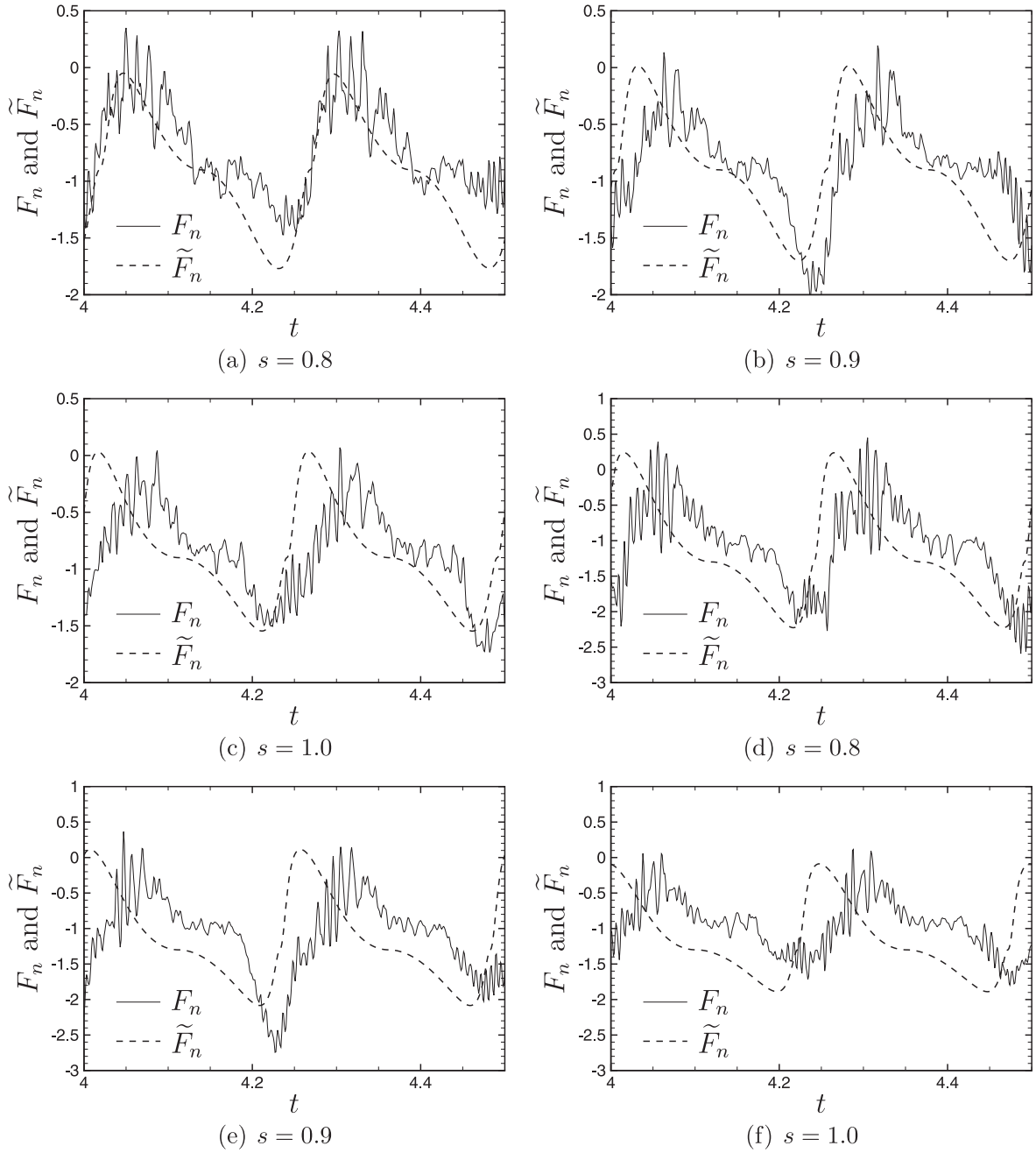

Figure 5. Force F_n on a tail section at abscissa s compared to $\widetilde{F}_n = \gamma |V_n| V_n$, where V_n is the normal velocity of the swimmer center line (the backbone). The parameter γ is adjusted to scale $\widetilde{F}_n$ with F_n. Top picture row, V_n is the local tangential velocity. Bottom row, V_n is taken at section $\Delta s = 0.05$ upstream.

homogeneous boundary condition on all boundaries. In all the following simulations we used the same domain $x \in [-2, 6]$, $y \in [-2, 2]$ and $z \in [-2, 2]$ with $h = 1/120$ and the mesh is composed by $8 \times 4 \times 4 \times 120^3 \approx 2.2 \times 10^8$ mesh nodes.

3.3. Force on caudal fin section

In the one-way elastic model that we have set up the force acting on the struts as $\widetilde{F}_n = \gamma |V_n| V_n$, where V_n is the normal speed of the swimmer centerline (the backbone). We compare the actual force F_n obtained for a self-propelling swimmer on a given section to $\widetilde{F}_n$. The force F_n is computed from equation (4) on the same section as $\widetilde{F}_n$. The computational set up corresponds identically to that of maximum efficiency of the next section. Three different sections are considered and the results are presented in figure 5. The top picture row shows the actual force computed on the given section versus the model force $\widetilde{F}_n$ on the same section. The model force is smoother but it is in substantial agreement with the actual force. The phase error is limited. The bottom picture row shows the same comparison for a model force $\widetilde{F}_n$ computed considering the normal velocity of a section that is $\Delta s = 0.05$ upstream. The overall deformation of the backbone will be modified and the swimming law will consequently vary. The phase error between the actual force experienced by each section considered and $\widetilde{F}_n$ increases, confirming the hypothesis the normal force locally scales like $|V_n| V_n$. We conclude that the simplified force model is a reasonable approximation of the actual force experienced by the swimmer. With this model the fluid–structure interaction is one way and this significantly simplifies the computational set up.

4. Efficiency

We set the kinematic viscosity $\nu = 10^{-3}$ m^2 s^{-1}. The swimmer is of unitary length $\ell = 1$ m and hence the swimming Reynolds number is 1000 V, where V the average swimming velocity. Such low Reynolds numbers are chosen so as to enable high resolution of the flow. We note that a swimmer swimming at a velocity of around one body-length per time unit, $Re = 10^3$ can be correlated to a small swimmer of 3 cm long.

4.1. Tail rigidity

As a first step in the analysis, for a given value of $\alpha = 0.1$, we have investigated how η varies as a function of k. By doing so, we modify the caudal fin flexibility and its characteristic frequencies. In the range $10^3 \leqslant k \leqslant 8 \times 10^3$ maximum efficiency is obtained for $k = 4 \times 10^3$, see figure 6. Indeed, for this value of k the tail amplitude oscillation for given forcing, is the largest compared to other values of k as seen in figure 6. This suggests that setting a value of k close to the structural model resonance leads to highest efficiencies. However, suboptimal values of k in terms of efficiency also lead to tail oscillation amplitudes that are very close to the largest.

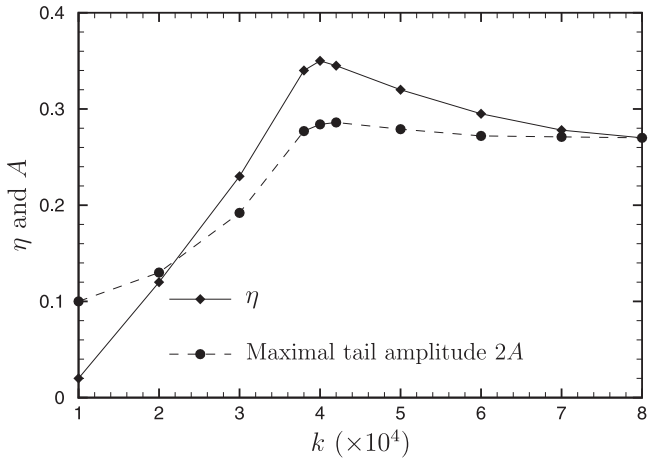

Figure 6. Evolution of the efficiency η and maximum tail amplitude $2A$ versus k.

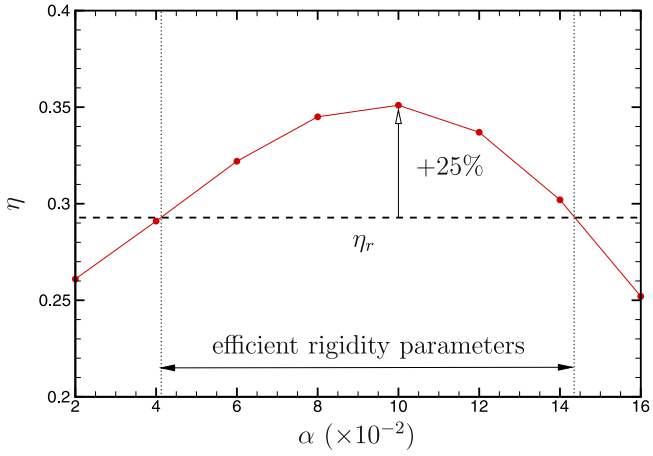

(a) η vs.α

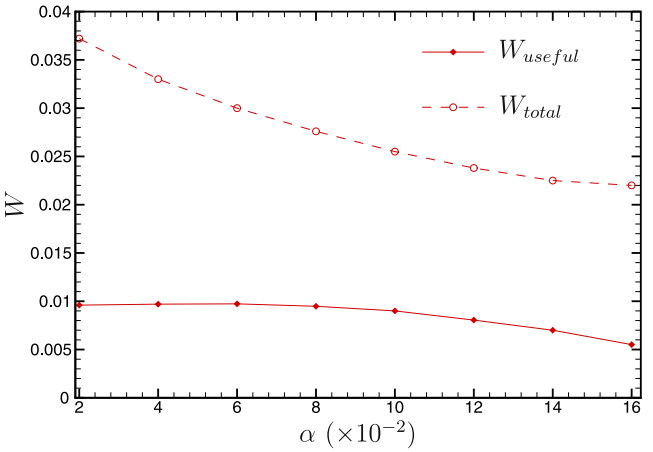

(b) W_{useful} and W_{total} vs. α

Figure 7. Evolution of the efficiency η, the useful work W_{useful} and the total work W_{total} versus the rigidity parameter α. The dotted line in the top figure corresponds to the imposed tail deformation.

We now explore, for given k, how efficiency varies as a function of α. We keep $k = 4 \times 10^3$ and we consider a range of the rigidity parameter α from 0.02 (low-flexibility tail) to 0.16 (high-flexibility tail). The parameter α is not directly

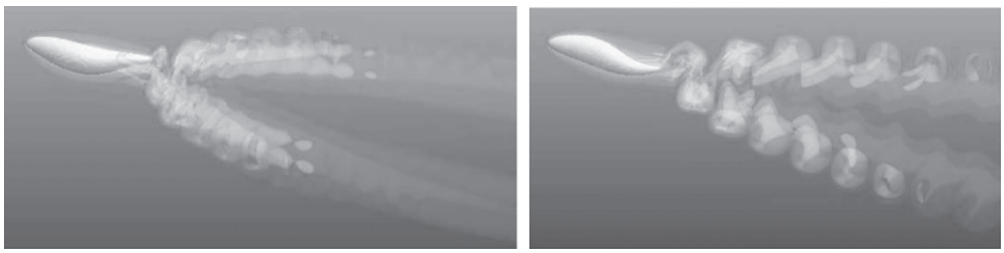

(a) $\alpha = 0.16$ (b) $\alpha = 0.10$

Figure 8. Vorticity snapshot of the wake generated by the modeled swimmer with $\alpha = 0.16$ and $\alpha = 0.1$ at Re $= 10^3$.

related to the elasticity modulus of a given material, that would be rather modeled by k. However, varying α we modify the structural model rigidity by keeping a fixed ratio between inertia and elastic forces so that the characteristic frequencies are unchanged. The variation of efficiency versus the parameter α for $f = 2$ Hz is shown in figure 7(a). We found that a value of $\alpha = 0.1$ maximize the efficiency and that the flexible tail increases the efficiency by about 25% in comparison to the case where the deformation is prescribed for the whole body. Figure 8 shows snapshots of the same vorticity field isocontours generated by the swimmer with maximum efficiency ($\alpha = 0.1$) and minimum efficiency ($\alpha = 0.16$). The swimmer generates a vortex street composed of two oblique rows of vortex rings, similar to that generated by a flapping foil (Dong *et al* 2006). This is characteristic of the wake generated for higher values of the swimming Strouhal number $St = \frac{f\,A}{V}$ (Dai *et al* 2012), typically for $St \geqslant 0.3$ (Borazjani and Sotiropoulos 2009). However, the wakes generated with $\alpha = 0.1$ and $\alpha = 0.16$ are qualitatively different. Indeed, the wake for $\alpha = 0.1$ presents a smaller angle between the two vortex rows, that can at least partially explain the production of reduced lateral forces (Wen and Lauder (2013) and references therein) in comparison with $\alpha = 0.16$. Here, the minimum swimming Strouhal number obtained for the swimming law considered is approximately 0.5.

A different definition of efficiency leads to similar results. As an example, we have employed the efficiency criteria in equation (9) introduced in Borazjani and Sotiropoulos (2008). This definition of efficiency results in the black curve depicted in figure 9. These results are compared to those obtained with the definition of this paper. It can be observed that optimality is reached for values of α that are close although the maximum is less pronounced.

In previous comparisons the swimmer velocity V was allowed to vary with α which introduced potentially confounding effects in the Reynolds numbers. In order to eliminate these effects, we have investigated the variation of the efficiency for a constant swimming velocity. In these cases, the frequency is kept at $f = 2.0$ Hz and the tail amplitude A is regulated by a proportional feed-back controller, see (Bergmann and Iollo 2011), to reach a target velocity of $V = 0.4$ m s^{-1}, which is the minimum velocity obtained for $\alpha = 0.16$. It happens that the tail excursion A is

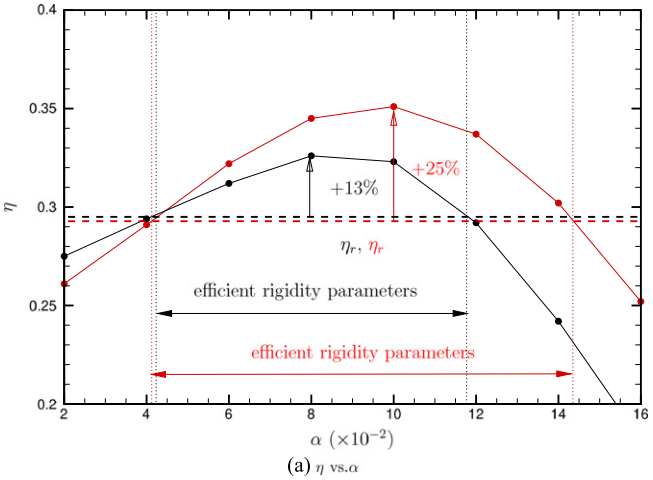

(a) η vs.α

Figure 9. Efficiency curves as a function of α. The black curve corresponds to the definition in equation (9) while the red curve corresponds to the definition of efficiency adopted in this paper. Dotted lines correspond to tail imposed deformation.

approximately constant for all values of α leading to a similar swimming Strouhal number. Figure 10(a) presents the evolution of the efficiency versus α and we find that $\alpha \geqslant 0.04$ produces a higher efficiency compared to the rigid tail. In fact, for $\alpha = 0.12$ the efficiency is increased by 35%. This quite high increase for $\alpha = 0.12$ can be explained by the increase of the useful work and the decrease of the total work over one stroke (see figure 10(b)).

4.2. Influence of tail curvature

In this section we investigate the influence of tail curvature on the swimming efficiency. We do that by varying the number of links in the tail. In the previous simulation we employed $N_L = 60$ links on the tail. In what follows, we take $1 \leqslant N_L \leqslant 5$ as presented in figure 11. The case $N_L = 60$ corresponds to $\alpha = 0.12$. and the parameter α is modified for $1 \leqslant N_L \leqslant 5$ so that the trajectory of the tail is as close as possible to the one for $N_L = 60$ with $\alpha = 0.12$. Note that the shape for $N_L = 5$ is similar to that with $N_L = 60$. Figure 12(a) shows that efficiency is enhanced when curvature is increased (N_L is increased). The evolution of the useful and total work versus the number of links N_L in presented in figure 12(b). While the value of the useful work is almost constant with N_L, the total work done by the swimmer

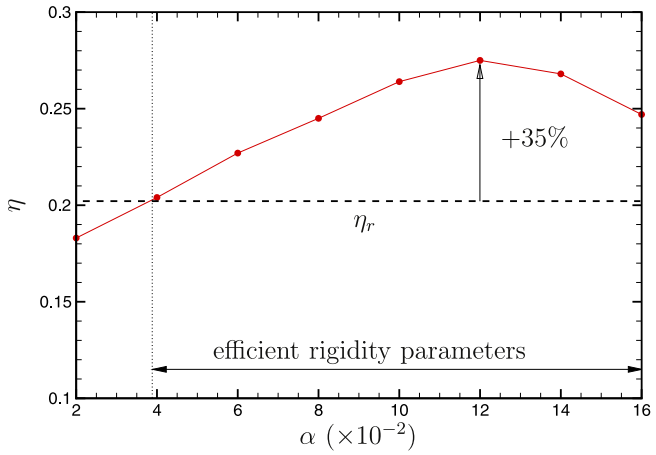

(a) η vs. α for $V = 0.4\,m.s^{-1}$

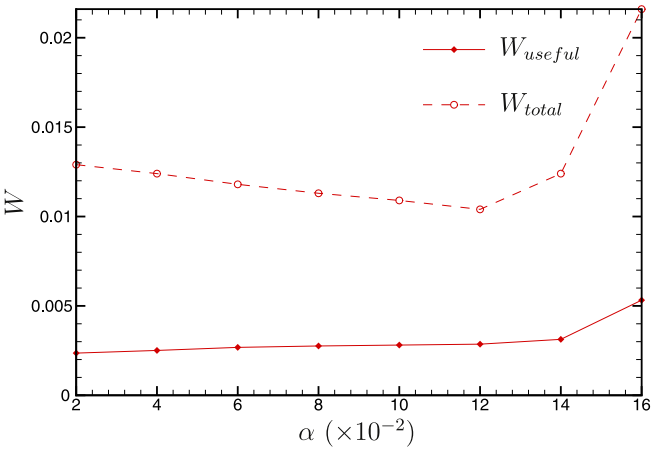

(b) W_{useful} and W_{total} vs. α for $V = 0.4\,m.s^{-1}$

Figure 10. Evolution of the efficiency η, the useful work W_{useful} and the total work W_{total} versus the rigidity parameter α for $V = 0.4$ m s^{-1}. The dotted line in the top figure corresponds to imposed tail deformation for $V = 0.4$ m s^{-1}

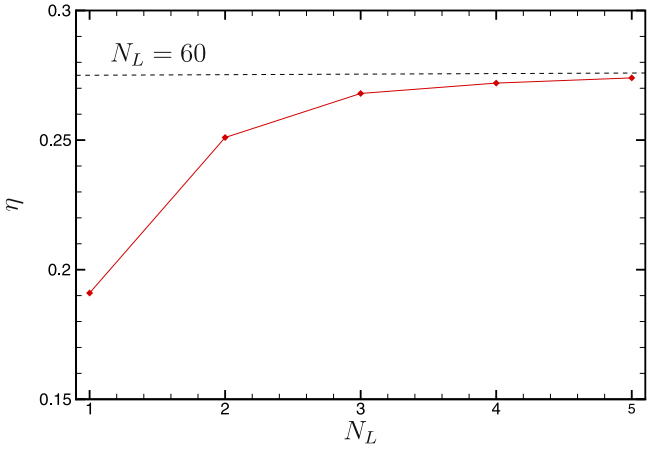

(a) η vs. N_L for $V = 0.4\,m.s^{-1}$

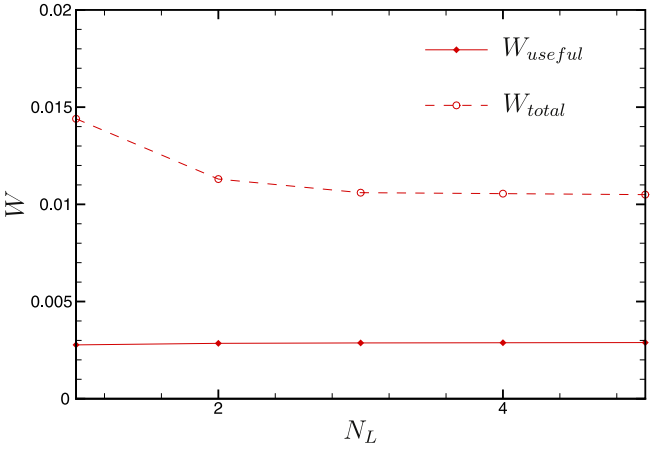

(b) W_{useful} and W_{total} vs. N_L for $V = 0.4\,m.s^{-1}$

Figure 12. Evolution of the efficiency η, the useful work W_{useful} and the total work W_{total} versus the number of links N_L for $V = 0.4$ m s^{-1}.

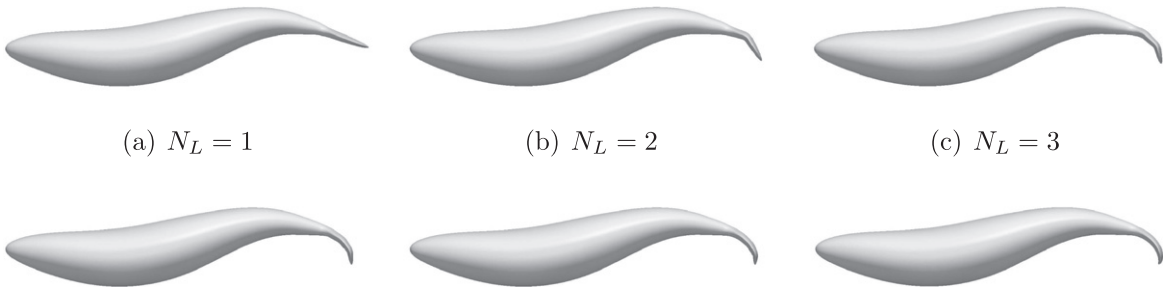

(a) $N_L = 1$ (b) $N_L = 2$ (c) $N_L = 3$

(d) $N_L = 4$ (e) $N_L = 5$ (f) $N_L = 60$

Figure 11. Swimmer shapes for different values of the number of links (N_L). The case $N_L = 60$ correspond to $\alpha = 0.12$.

over one stroke decreases with increasing N_L and eventually reaches the value obtained for our test case with $N_L = 60$. An optimal value of the flexural rigidity help to decrease the work done by the swimmer, especially the contribution due to the lateral motion. Indeed, when the swimmer velocity is constant, the total work is equal to the work done by the lateral motion.

5. A simple model for tail design

The largest forces and velocities on the swimmer are located on the tail. Let us consider the local contribution of the useful work $\overline{W}_{\text{useful}}(x)$ relative to each section normal to the midline at abscissa x. We define by $W_x = 100\,\frac{\overline{W}_{\text{useful}}(x)}{W_{\text{useful}}}$ the percentage

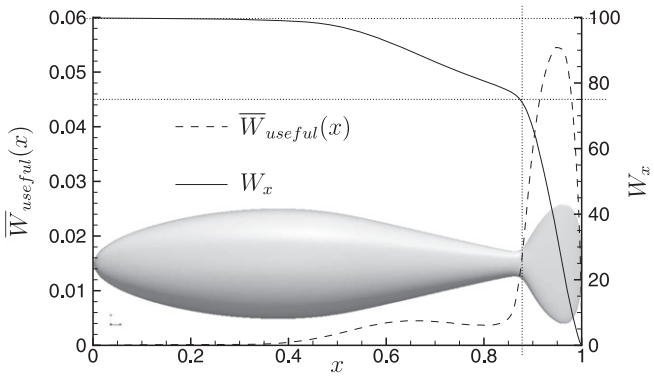

Figure 13. Evolution of the local useful work contribution along the midline and and overall useful work generated starting from the caudal fin.

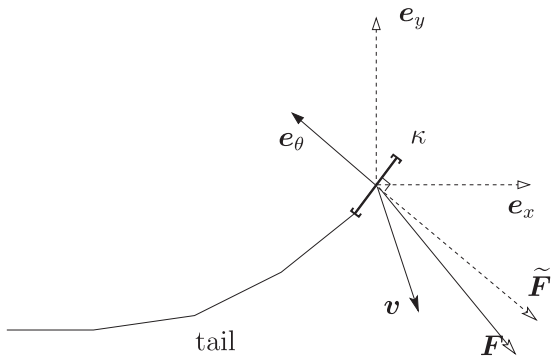

Figure 14. Sketch of the tail in the simplified efficiency model.

of the useful work generated between abscissa x and 1. In figure 13 we see that 75% of the total useful work is contributed by the caudal fin, i.e., the last 12% of the swimmer. Hence, in order to obtain a simple interpretation of flow physics underlying our observations of efficiency enhancement, we now focus only on the tail segment, denoted by κ. Let $\boldsymbol{e}_\theta$ be the normal to κ as in figure 14. The relative velocity of the mid point of κ with respect to swimmer velocity is denoted by $\boldsymbol{v} = (v_x,\ v_y)$ and let the force exerted by κ on the fluid be $\boldsymbol{F}$. The normal component of this force is mainly generated by the pressure jump, whereas the tangential force is generated by viscous effects. As a first approximation, we neglect the viscous contributions since the Reynolds number is relatively high. In this limit, we model the force by $\widetilde{\boldsymbol{F}} = (f_x,\ f_y) = \chi(\boldsymbol{e}_\theta \cdot \boldsymbol{v})|\boldsymbol{v}|\boldsymbol{e}_\theta$, where $\chi > 0$ is areal constant. Thrust is generated when $f_x > 0$. The useful work is then $\widetilde{W}_{\text{useful}} = \int_T \frac{f_x + |f_x|}{2} v_x \mathrm{d}t$, the work generated by lateral motion is $\int_T f_y\ v_y \mathrm{d}t$ and the total work is $\widetilde{W}_{\text{total}} = \int_T \widetilde{\boldsymbol{F}} \cdot \boldsymbol{v} \mathrm{d}t$. The efficiency resulting from this model is then $\widetilde{\eta} = \frac{\widetilde{W}_{\text{useful}}}{\widetilde{W}_{\text{total}}}$.

Figure 15(b) shows the evolution of $\widetilde{W}_{\text{useful}}$ and $\widetilde{W}_{\text{total}}$ versus α. We scaled β as $\beta = 0.06$ so that the useful and total work are in the same ranges as in figure 7(b). The tendencies are similar to those obtained in figure 15(b), except for the largest values of α. The plot of $\widetilde{\eta}$ versus α is presented in figure 15(a). Even if the values of $\widetilde{\eta}$ are slightly different from that of η obtained in figure 7(a), the overall trends are found to be similar. Indeed, the maximum efficiency is obtained for the same value of α (= 0.12) in both cases.

In figure 16 we show the trajectory of κ and the corresponding model forces as a function of the tail rigidity. For rigid tails ($\alpha = 0.02$) the forces are propulsive over the whole cycle but they are small in intensity and have large vertical components. For optimal rigidity ($\alpha = 0.10$) the forces are propulsive over most of the cycle; their modulus is comparatively large and the vertical components are small. For high flexibility ($\alpha = 0.16$) the modulus of the vertical forces is large and the horizontal force is drag-generating over nearly half of the cycle. For this last case, the integral contribution over one period of the forces in the x direction becomes negative. This simplified analysis is in

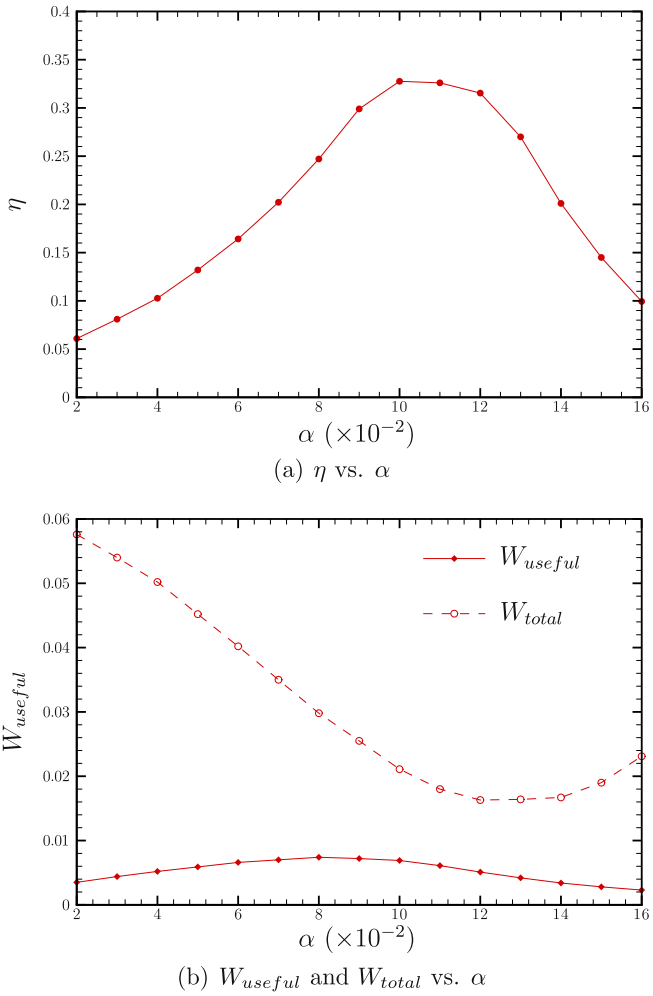

Figure 15. Evolution of the efficiency $\widetilde{\eta}$, the useful work $\widetilde{W}_{\text{useful}}$ and the total work $\widetilde{W}_{\text{total}}$ versus the rigidity parameter α. The dotted line corresponds to the imposed tail deformation.

accordance with observations done for figure 8, where the angle between the vortex rows is smaller in the most efficient swimmer.

6. Conclusions

The effect of tail flexibility on swimming performance has been examined via Navier–Stokes simulations coupled with a

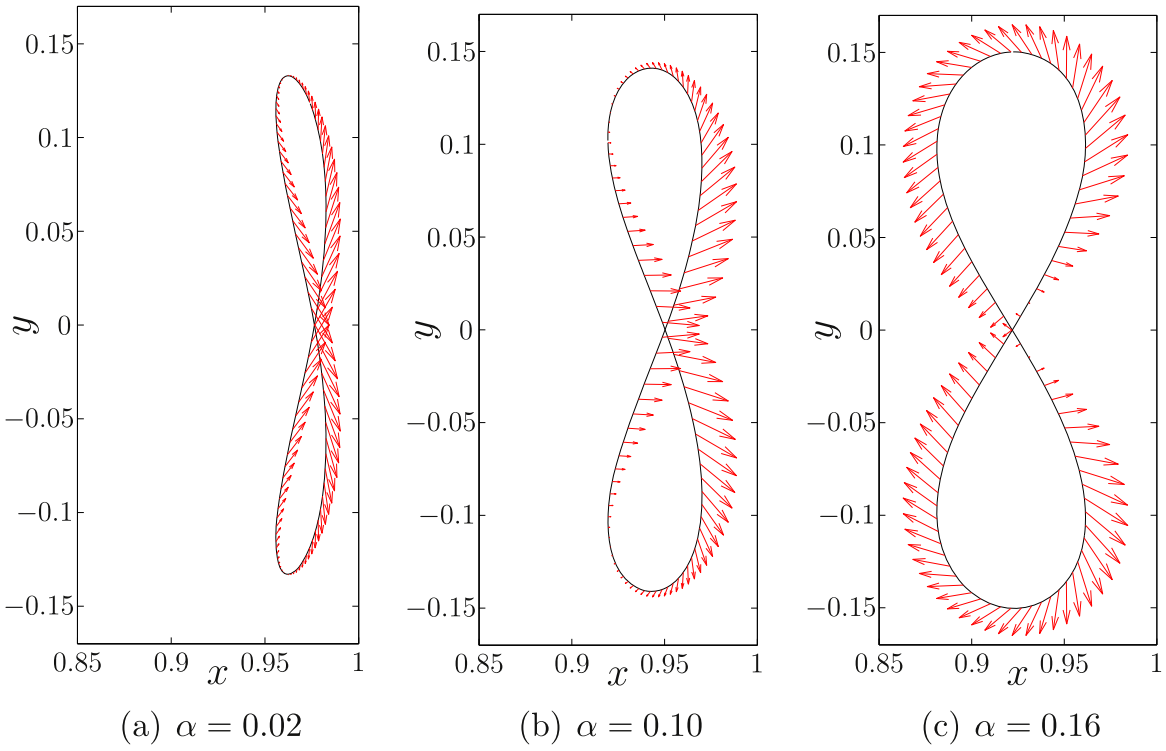

Figure 16. Trajectory of κ mid-point and corresponding force $\widetilde{\boldsymbol{F}}$ for different values of α.

lumped-element model of the flexible caudal fin. Our results show that allowing caudal fin deformation induced by a simple elastic model has a marked influence on the propulsive performance of the swimmer.

The one-way fluid–structure interaction model shows that optimal efficiency is obtained for an intermediate flexibility of the caudal fin and that neither excessive rigidity nor compliance are conducive to efficient propulsion. We further show that a limited number of links (≈3) in the tail is able to generate tail curvatures sufficient to reach efficiencies obtained with a larger number of links. Our investigation is valid for low Reynolds number regimes and without taking into account possible skin effects (like polymer release) or small-scale compliant-tissue effects. Although these results are obtained in the limits of a one-way coupling, it is expected that they are not qualitatively affected by the simplifications in the structural model. It is shown indeed that the actual force experienced by the swimmer tail is reasonably approximated by the model. Furthermore, an interpretation of these results is given based on a purely kinematic model. We observe that rigid caudal fins lead to excessive lateral forces that increase power consumption without generating thrust, whereas highly flexible caudal fins produces negative thrust during significant portions of the stroke. These results may lead to significant improvements in the design of underwater robots and suggest bioinspired designs for flexible fin swimmers.

In this work, changing the caudal fin model parameters is equivalent to changing the kinematics of the tail, mimicking the effects of actual fluid forces. A precise study on the part of performance improvement due to kinematics optimization versus elastic energy recoil could be shown by comparing a two-way coupling with a flexible tail, to a similar prescribed tail kinematics.

Analysis of the flow features in the wake of the swimmer does not allow to uncover a mechanism which would clearly explain the efficiency gain obtained when varying the structural model parameters. No evident phenomena occur in the wake flow topology explaining this improvement. An explanation proposed here is that the detailed kinematics of the flapping tail explains, at least partially, this effect. With respect to the literature, we also observe that resonance, interpreted as configurations for which the largest tail amplitudes are induced by the same forcing, only partially explain the increase of efficiency. Indeed, a clear maximum in efficiency is obtained for values of k that give very simular maximum tail amplitudes. It is probably accurate to state that optimum efficiency results from a careful combination of resonance combined with an appropriate tail kinematics that results in the most favorable hydrodynamic configuration for propulsion.

Acknowledgments

This study has been carried out with financial support from the French State, managed by the French National Research Agency (ANR) in the frame of the ‘Investments for the future’ Programme IdEx Bordeaux-CPU (ANR-10-IDEX-03-02). The simulations presented in this paper were carried out using the PLAFRIM experimental parallel testbed, being developed under the Inria PlaFRIM development action with support from LABRI and IMB and other entities: Conseil

Régional d'Aquitaine, FeDER, Université de Bordeaux and CNRS (see https://plafrim.bordeaux.inria.fr/).

References

Angot P, Bruneau C and Fabrie P 1999 *Numer. Math.* **81** 497–520
Barrett D, Triantafyllou M, Yue D, Grosenbauch M and Wolfgang M 1999 *J. Fluid Mech.* **392** 182–212
Bergmann M and Iollo A 2011 *J. Comput. Phys.* **230** 329–48
Borazjani I and Sotiropoulos F 2008 *J. Exp. Biol.* **211** 1541–58
Borazjani I and Sotiropoulos F 2009 *Phys. Fluids* **21** 091109
Bose N 1995 Performance of chordwise flexible oscillating propulsors using a time-domain panel *Int. Shipbuild. Prog.* **42** 281–94
Chorin A 1968 *Math. Comput.* **22** 745–62
Clift R, Grace J R and Weber M E 1978 *Bubbles, Drops and Particles* (New York: Academic)
Coquerelle M and Cottet G 2008 *J. Comput. Phys.* **227** 9121–37
Curet O M, AlAli I K, MacIver M A and Patankar N A 2010 *Comput. Methods Appl. Mech. Eng.* **199** 2417–24
Dai H, Luo H, de Sousa P J S A F and Doyle J F 2012 *Phys. Fluids* **24** 101903
Dong H, Bozkurttas M, Mittal R, Madden P and Lauder G 2010 *J. Fluid Mech.* **645** 345–73
Dong H, Mittal R and Najjar F M 2006 *J. Fluid Mech.* **566** 309
Esposito C J, Tangorra J L, Flammang B E and Lauder G V 2011 *J. Exp. Biol.* **215** 56–67
Fish F and Lauder G 2006 *Annu. Rev. Fluid Mech.* **38** 193–224
Gazzola M, Chatelain P, van Rees W M and Koumoutsakos P 2011 *J. Comput. Phys.* **230** 7093–114
Glowinski R, Pan T W, Hesla T, Joseph D and Priaux J 2001 *J. Comput. Phys.* **169** 363–426
Heathcote S, Wang Z and Gursul I 2008 *J. Fluids Struct.* **24** 183–99
Hieber S and Koumoutsakos P 2008 *J. Comput. Phys.* **227** 8636–54
Katz J and Weihs D 1978 *J. Fluid Mech.* **88** 485–97
Lauder G V, Madden P G A, Mittal R, Dong H and Bozkurttas M 2006 *Bioinspir. Biomim.* **1** 25–34
Liu W, Xiao Q and Cheng F 2013 *Bioinspir. Biomim.* **8** 036011
Marais C, Thiria B, Wesfreid J E and Godoy-Diana R 2012 *J. Fluid Mech.* **710** 659–69
Masoud H and Alexeev A 2010 *Phys. Rev.* E **81** 056304
McCutchen C 1970 *J. Biomech.* **3** 271–81
Mittal R, Dong H, Bozkurttas M, Najjar F, Vargas A and von Loebbecke A 2008 *J. Comput. Phys.* **227** 4825–52
Mittal R and Iaccarino G 2005 *Annu. Rev. Fluid Mech.* **37** 239–61
Prempraneerach P, Hover F and Triantafyllou M 2003 *13th Int. Symp. Unmanned Untethered Submersible Technology* (NH: Durham)
Ramamurti R, Sandberg W C, Löhner R, Walker J A and Westneat M W 2002 *J. Exp. Biol.* **205** 2997–3008
Ramananarivo S, Godoy-Diana R and Thiria B 2011 *Proc. Natl. Acad. Sci.* **108** 5964–9
Sfatiotakis M, Lane D and Lane D J B 1999 *IEEE J. Ocean. Eng.* **24** 237–52
Shirgaonkar A A, MacIver M A and Patankar N A 2009 *J. Comput. Phys.* **228** 2366–90
Spagnolie S E, Moret L, Shelley M J and Zhang J 2010 *Phys. Fluids* **22** 041903
Thiria B and Godoy-Diana R 2010 *Phys. Rev.* E **82** 015303
Triantafyllou M, Triantafyllou G and Yue D 2000 *Ann. Rev. Fluid Mech.* **32** 33–53
Vanella M, Fitzgerald T, Preidikman S, Balaras E and Balachandran B 2009 *J. Exp. Biol.* **212** 95–105
Vermeiden J, Kooiker K, Lafeber F, van Terwisga T, Cerup-Simonsen B and Folso R 2012 *29th Symp. on Naval Hydrodynamics* (Sweden: Gothenburg)
von Loebbecke A, Mittal R, Fish F and Mark R 2009 *J. Biomech. Eng.* **131** 054504
Wen L and Lauder G 2013 *Bioinspir. Biomim.* **8** 046013
Wiens A J and Nahon M 2012 *Bioinspir. Biomim.* **7** 046016
Young J, Walker S M, Bomphrey R J, Taylor G K and Thomas A L 2009 *Science* **325** 1549–52
Zhu Q, Wolfgang M, Yue D and Triantafyllou M 2002 *J. Fluid Mech.* **468** 1–28